

Grain Boundaries as Electrical Conduction Channels in Polycrystalline Monolayer WS₂

Yingqiu Zhou,¹ Syed Ghazi Sarwat,¹ Gang Seob Jung², Markus J. Buehler,^{2,3} Harish Bhaskaran,¹ Jamie H. Warner^{1*}

¹Department of Materials, University of Oxford, Parks Road, Oxford, OX1 3PH, United Kingdom

² Laboratory for Atomistic and Molecular Mechanics (LAMM), Department of Civil and Environmental Engineering, Massachusetts Institute of Technology, 77 Massachusetts Ave., Cambridge 02139, MA, USA

³Center for Computational Engineering, Massachusetts Institute of Technology, 77 Massachusetts Ave., Cambridge, MA 02139, USA

Email: *Jamie.warner@materials.ox.ac.uk;

Abstract

We show that grain boundaries (GBs) in polycrystalline monolayer WS₂ can act as conduction channels with a lower gate onset potential for field effect transistors (FETs) made parallel, compared to devices made in pristine areas and perpendicular to GBs. Localized doping at the GB causes photoluminescence quenching and a reduced Schottky barrier with the metal electrodes, resulting in higher conductivity at lower applied bias values. Samples are grown by chemical vapour deposition with large domains of ~100 μm, enabling numerous devices to be made within single domains, across GBs and at many similar sites across the substrate to reveal similar

behaviors. We corroborate our electrical measurements with kelvin probe microscopy (KPM), highlighting the nature of the doping-type in the material to change at the grain boundaries. Molecular dynamics simulations of the GB are used to predict the atomic structure of the dislocations and meandering tilt GB behavior on the nanoscale. These results show that GBs can be used to provide conduction pathways that are different to transport across GBs and in pristine area for potential electronic applications.

KEYWORDS: WS₂, grain boundaries, threshold voltage, kelvin probe microscopy, photoluminescence

Introduction

Discovery of graphene in 2004 led to a interest in materials beyond silicon for semiconductor technologies^{1,2} particularly for flexible and wearable technologies, due to its high carrier mobility,^{2,3} broad-band absorption,^{4,5} high transparency,^{4,6} and ultrathin gemomerty.^{2,7} Nevertheless, graphene lacks an intrinsic band-gap and this leads to high leakage current for transistor applications,^{8,9} hindering its direct-use as channels for transistors that underpin many electronic and optoelectronic technologies. Another class of two dimensional materials called the transition metal dichalcogenides (TMDs) are a group of semiconductors with intrinsic bandgaps that have gained traction for ultrathin semiconductor technologies.^{10–13,38} One of the appealing properties of TMDs is that their bandgap is thickness dependent,^{10,12,14} which makes it possible to tune the properties of TMDs by controlling layer number. MoS₂ and WS₂ are two of the most studies materials in the TMD family with their energy bandgap ranging from visible to the near-infrared region.^{11,12} Due to their interesting properties, they have great potential in next generation nanoelectronics and opto-electronics, such as integrated logic circuits, phototransistors, field-effect transistors and flexible optoelectronic devices.^{15–19}

These applications have been significantly facilitated by the progress of synthesis methods for scalable TMD production. Chemical vapour deposition (CVD) is one of the widely adopted approaches to overcome the large scale synthesis challenge.^{20,21,39} However, with this method, a large number of defects are introduced into the crystal domains of the two dimensional materials and the polycrystalline thin films. These defects have been regarded as one of the main factors for the reduced device performances. For example, the carrier mobility of CVD grown MoS₂ typically range between $\sim 0.004\text{-}0.4\text{cm}^2\text{V}^{-1}\text{s}^{-1}$, an order of magnitude smaller compared to the mechanically exfoliated ones ($0.3\text{-}5\text{cm}^2\text{V}^{-1}\text{s}^{-1}$).²² Grain boundary (GB) is a most prominent defect in polycrystalline CVD synthesized two dimensional TMDs.²³⁻²⁵ It has therefore become imperative to understand its features and the effect it brings to the different properties, not only for better regulation of device fabrication, but also for potential applications of GBs.

The atomic structure of TMDs is commonly studied with transmission electron microscopy (TEM).^{23,25} 5|7 and 8|4 dislocation cores are observed to be the primary defects of GBs,²³⁻²⁵ depending on the type of the GB. Scanning tunneling electron microscopy (STEM) and other optical microscopies have also been used to study the GB.^{23,25} Theoretical calculations, including Density Functional Theory (DFT) predict that at grain boundaries the electronic states are altered either through induced stress or broken atomic periodicity.²⁴ Furthermore, the inter-domain electrical properties of MoS₂ have been discovered to be not only closely related to the types of GBs, but also influenced by the misorientation angle between domains.²⁴ While a great deal of research has been put into understanding the influence of GBs on the mechanical properties of two dimensional materials, the understanding of the impact GBs have on the carrier transport in TMDs remains less explored.²³ Studies to date have focused on transport across the GBs, without exploring the transport phenomena along the GB lines.

Here, we study field effect transistor (FET) performance in high quality CVD grown uniform monolayer WS₂ domains with an average domain size up to 100 μm , containing merged domain regions with known mirror GB locations that can be detected using optical microscopy. We examine the charge carrier transport behavior of FETs built parallel to GBs and compare it to pristine and perpendicular aligned devices. Optical spectroscopy and nanoscale kelvin probe microscopy are used to support the conductivity measurements.

Results and Discussions

The WS₂ domains are synthesized using a previously reported CVD method.²⁶ With this method, uniform WS₂ domains with large scale and high density can be grown on SiO₂ (300nm)/Si substrate. The GBs formed between monolayer WS₂ domains are visible under optical microscope with proper optical contrast optimization while some are invisible. **Figure 1a** shows truncated WS₂ domains with average size up to 100 μm spread across the substrate. **Figure 1b** is the SEM image of triangular WS₂ monolayer domains. Two of the GBs with darker color are very easy to locate, which are marked with red arrows. The different shapes of WS₂ in **Figure 1a** and **b** are due to the different growth kinetics that occur in different locations on the SiO₂/Si substrate²⁷. By analyzing the direction of the visible GBs relative to the WS₂ domain orientation, we find that these GBs start along the bisector angle between two WS₂ domains regardless their relative orientation, as illustrated in **Figure 1b**. The mirror property of visible GBs is similar to the invisible ones reported.²⁸ The GBs bend to different directions to fit the orientation and center separation distance of the WS₂ domains, as shown in **Figure 1c-e**.

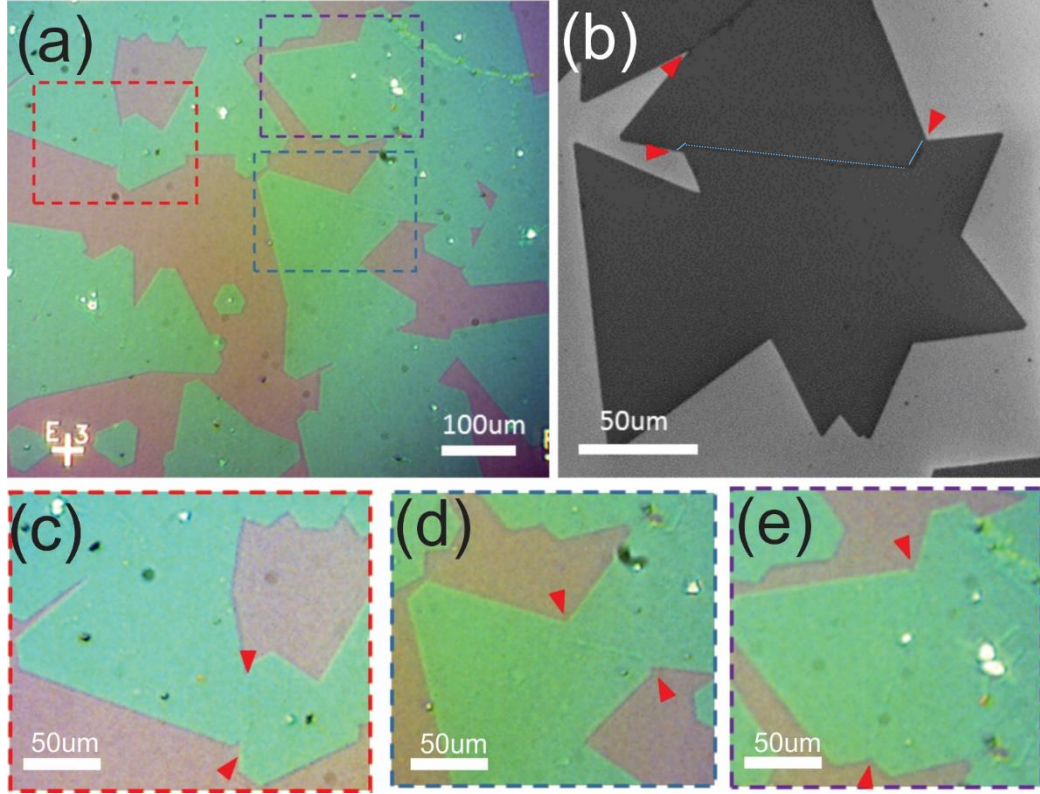


Figure 1. Visible GBs observed in the CVD synthesized monolayer WS_2 (a) Optical image of monolayer WS_2 domains on SiO_2/Si substrate. (b) SEM image of monolayer WS_2 domains merging to form visible GBs. The red arrows point to the visible GBs and the GBs are indicated by dotted blue lines. (c-e) Optical images of WS_2 GBs of different configurations and angles. The red arrows pointed to the GBs.

The optical properties of a visible GB formed between two WS_2 domains of 19.5° orientation mismatch is studied by photoluminescence and Raman spectroscopy. **Figure 2a** is the Raman spectra of the pristine WS_2 . **Figure 2b** is the optical image showing that two WS_2 domains merge together to form a GB. Based on the GB, field effect transistors were fabricated to study the influence of the GB on the electrical properties of monolayer WS_2 . Based on the relative orientation between the conducting channel and the GB, transistors of three different types were fabricated: with GB (a) with GB perpendicular to the channel (GB_\perp), (b) with GB parallel to the channel (GB_\parallel) and without GB (pristine).

CVD synthesized WS_2 was first transferred onto SiO_2 (300nm)/Si substrate with the assistance of a PMMA scaffold. Electron-beam lithography and oxygen plasma were used to pattern and etch the WS_2 into ribbons along GBs with 10 μm width. Cr (20nm)/Au(80nm) was subsequently deposited onto the patterned WS_2 ribbon as electrodes with channel length as 10 μm using thermal evaporation method. **Figure 2c** is the SEM image of a typical device with the three different GB orientations. In the SEM image, the white contrast highlighted by the red arrows is the GB. In order to examine the optical properties of the GB in the device, photoluminescence mapping of the WS_2 was carried-out, which is shown in **Figure 2d**. There is strong PL quenching along the GB as indicated on PL mapping image. The integrated intensity at the GBs quenches significantly (1/3 to that of monolayer WS_2) as shown in **Figure 2e**. Using Lorentzian fitting, the PL spectra at GB and pristine WS_2 have been fitted for two peaks, corresponding to the exciton (X) and negative trion (X^-), respectively, as shown in **Figure 2f**. For the pristine WS_2 , the exciton and trion peaks are located at around 2.00eV and 1.975eV, respectively. The high trion peak intensity suggests n-doping of WS_2 . The increased intensity ratio of X^-/X from 4.5 to 8 at the GB suggests a higher n-doping at the GBs. This likely stems from sulfur deficiency (sulfur vacancy) at the GBs, which is prevalent in CVD synthesized TMDs²⁹ or due to the strain induced modifications.³⁰

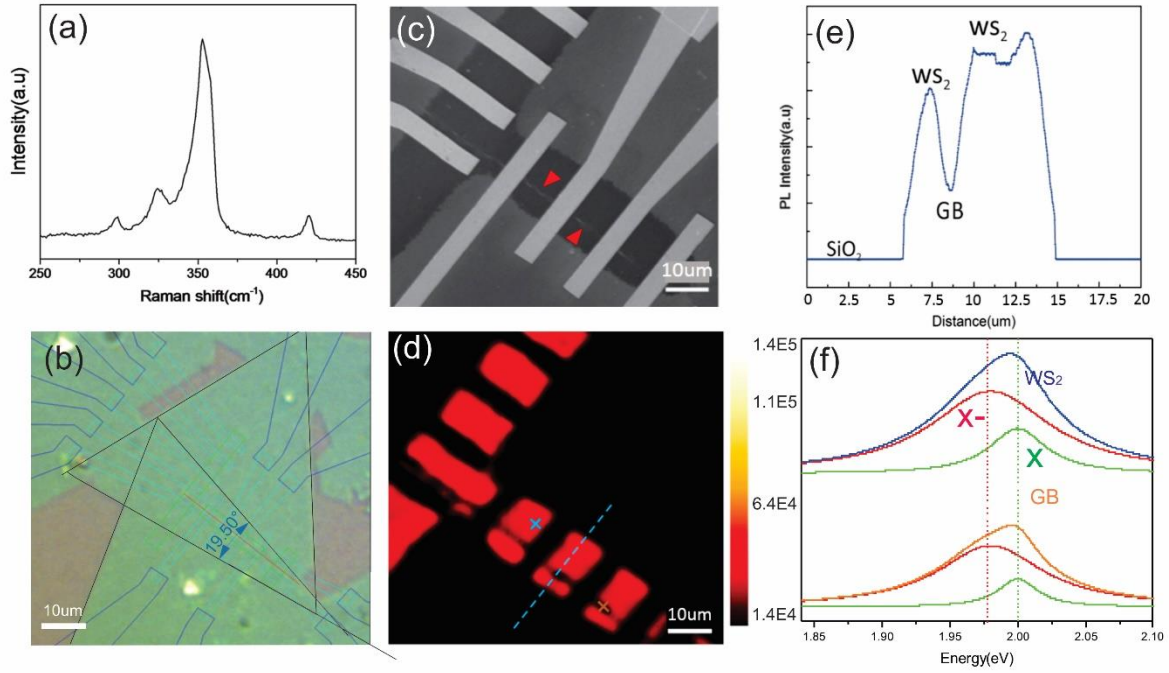


Figure 2. (a) Raman characterization of monolayer WS_2 away from the GB. (b) The optical image showing two monolayer WS_2 domains merging together to form GB. The black triangles represent the outline of two WS_2 domains. The green and blue outlines are the designed electrodes for device fabrication around the GB. (c) SEM image of the WS_2 devices based on the design shown in (b). (d) PL mapping spectrum of the WS_2 GB by integrating the photo emission intensities from energy of 1.85eV to 2.10eV. (e) PL integrated intensity line profile corresponding to the line marked in (d) showing obvious PL quenching along the GB. (f) Lorentzian fitting of the PL spectra of both monolayer WS_2 and GB.

$I_{\text{sd}}\text{-}V_{\text{sd}}$ measurements are carried on the three sets of devices. Electrical properties of two dimensional materials are known to be very sensitive to adsorbates (H_2 , O_2 and H_2O)^{31,32}. Before every electrical measurement, the devices were left in a vacuum chamber for around 4 hours at low pressure $\sim 3 \times 10^{-8}$ bar to enable desorption of absorbed molecules. Joule annealing was then carried-out to further improve desorption³⁶ and improve adhesion of WS_2 with the metal contacts.³⁷ All the electrical measurements were performed at room temperature and in dark conditions. **Figure 3a-c** show the $I_{\text{sd}}\text{-}V_{\text{sd}}$ characteristics from multiple transistors with and without GBs under various V_g . The results in **Figure 3a** and c show that the devices with GBs in the channel are

conductive and undergo electrostatic induced modulations. The I_{sd} - V_{sd} plots show a nonlinearity indicating Schottky contacts at the interface of metal and WS_2 . When V_g is increase from -4V to 16V, I_{sd} in all three devices is found to increase. The gate dependent measurements reveal that the devices with GBs in the channel can still be tuned effectively by the back-gate voltage regardless of the relative orientation of the GBs to the channel direction. It is to be noted however that the current in the WS_2 +GB $_{//}$ devices is doubled compared with devices with the pristine WS_2 devices at high V_{ds} . This improvement indicates that GB is more conductive than pristine monolayer WS_2 . This behavior can be attributed to reduced Schottky barrier between metal contact and GB³³, which likely arises from increased n-doping at the GB, which has been observed in the PL spectrum.

In **Figure 3d** and **e**, we compare the transfer characteristics (I_{ds} - V_g) of these three sets of devices. An n-type behavior is observed in the I_{ds} - V_g plots for all of the three devices. However, it is to be noted that the existence and the orientation of the GBs influences significantly the value of the threshold voltages (V_{th}). The V_{th} here is extrapolated in the linear region of the transfer characteristic curve.³⁴ For the devices based on pristine WS_2 , the average V_{th} is found to be 11 V. Existence of a GB parallel to the channel reduces (negative shift) the V_{th} by 7 V to around 4 V, while the existence of perpendicular GB (WS_2 +GB $_{\perp}$), the average V_{th} is found to be 17 V (positive shift by 6V), as shown in **Figure 3f**. The negative shift of V_{th} for WS_2 +GB $_{//}$ device indicates that the energy band of the WS_2 GBs shifts down. Due to the band bending, the effective Schottky barrier between the contact metal and GBs decreases, allowing the device to operate at a lower gate voltage than the one without GBs. Furthermore, the field-effect mobility for the three sets of devices are extracted at the maximum transconductance in the linear regime using the equation:

$$\mu_{FE} = \frac{1}{C_i} \frac{L}{W} \left(\frac{dI_{ds}}{dV_{bg}} \right) \frac{1}{V_{ds}} \quad (\text{Eq.1})$$

Where L and W are the length (10 μm) and width (10 μm) of the conductive channel, respectively. C_i is the capacitance per unit area of the 300nm thick SiO_2 (11.6nF cm^{-2}). I_{ds} , V_{ds} and V_{bg} are the source-drain current, source-drain voltage and back-gate voltage, respectively. For the pristine devices, the mobility varies from 0.12 to 0.47 $\text{cm}^2 \text{V}^{-1}\text{s}^{-1}$. The low mobility is probably due to the substrate roughness and charge scattering from defects. The mobilities for the $\text{WS}_2+\text{GB}_{//}$ and $\text{WS}_2+\text{GB}_{\perp}$ devices are calculated to be around 0.2 and 0.4 $\text{cm}^2 \text{V}^{-1}\text{s}^{-1}$, which is within the variation range of the mobility of pristine WS_2 devices in our study. This indicates that the existence of the GB does not bring much difference to the field-effect mobility to the WS_2 devices. Mobility is strongly affected by the intrinsic and extrinsic scattering centers of the channel. The intrinsic defects generated in WS_2 during the CVD synthesis process and the extrinsic scattering centers exist between the conductive channel and substrate bring more degradation to the mobility than that caused by GB.

The decreased threshold voltage in $\text{WS}_2+\text{GB}_{//}$ device indicates an increase of charge carrier density along the GB at gate voltages less than required for bulk WS_2 . Using the equation: $n = \epsilon_0 \epsilon_r \Delta V_T / te$,³⁵ we estimate the charge carrier density induced at the GB. Where ϵ_0, ϵ_r are the dielectric constants of free space ($8.85 \times 10^{-12} \text{F/m}$) and SiO_2 (3.9) respectively; ΔV_T is the average difference of the threshold voltage between the pristine WS_2 devices and the $\text{WS}_2+\text{GB}_{//}$ devices; t is the thickness of SiO_2 dielectric layer (300nm); e is the electron charge ($1.6 \times 10^{-19} \text{C}$). The charge carrier density at which the channel becomes conductive due to the presence of the GBs is calculated to be $5 \times 10^{11} \text{cm}^{-2}$ on average.

A logarithmic $I_{\text{ds}}-V_g$ plot is shown in the **Figure 3e**. It can be seen that all three sets of devices show comparable on/off ratio of around 10^3 , with off-current as low as 0.1nA. The off current we observed here is similar for the devices with parallel GBs and those without GBs, which

is likely due to the much larger width of the pristine WS_2 ribbon compared with that of the GB wire in the channel. The off current is influenced by the Schottky barrier for the minor carrier (holes in our case). As the Schottky barrier for electrons in GBs is lower than that in pristine WS_2 , the Schottky barrier for holes in GBs is higher than that in pristine WS_2 . The off current contributed by GBs is thus smaller than that from pristine WS_2 with the same width. But the width of GBs is much smaller than that of WS_2 ribbons, the decrease of the off current induced by GBs is not detectable in our measurement. The subthreshold voltages are calculated to be 1.8V/dec and 1.7V/dec for pristine WS_2 based devices and $\text{WS}_2+\text{GB}_\perp$ devices, respectively. While for the $\text{WS}_2+\text{GB}_\parallel$ devices, the sub-threshold swing (SS) is more than doubled (3.99V/dec). The subthreshold transport is understood to be dominated by carrier diffusion across the channel. The increase in the SS can be due to increased charge scattering centers that arise from both GB and defects at the interfaces. This effect is naturally expected to be more pronounced for GBs parallel to the channel, due to increased concentration of scattering defects.

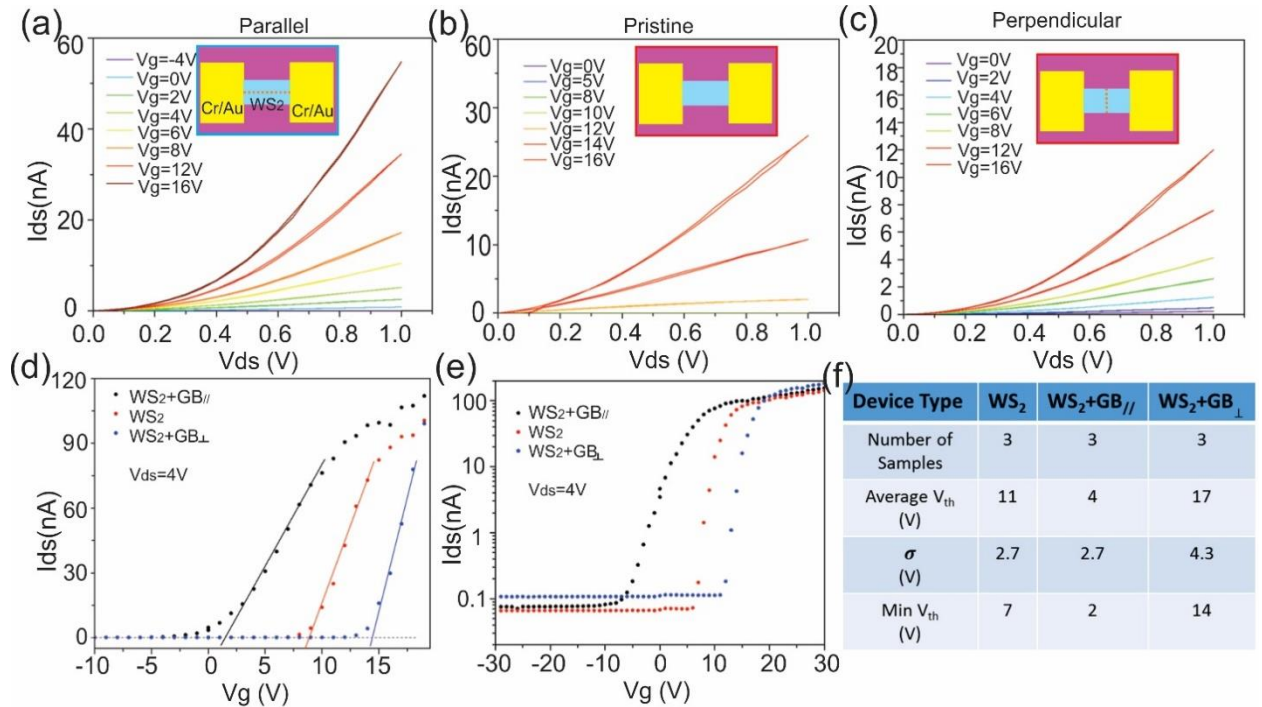


Figure 3. Electrical characterization of field-effect transistors with conductive channels parallel to GBs, with pristine WS₂ and perpendicular to the GBs in dark and vacuum condition. (a-c) Plots of the I_{ds} - V_{ds} curves of devices of three different structures under various gate voltages during the forward sweep. (d) Transfer curves of devices of three structures at a bias voltage at 4 V. (e) Semilogarithmic plots of the curves in (d). (f) Comparison of the threshold voltage (V_{th}) of devices with three different structures. 3 devices of each structure are measured. The average, variance and minimum V_{th} are presented in the table.

So far our electrical measurements have indicated that the GBs influence the charge transport characteristics, which could likely be a result of differential doping levels between the bulk and the GBs as indicated on PL spectra earlier. In order to further support this, the surface potentials were measured at the GB and the pristine areas of WS₂ using Kelvin probe microscopy (KPM). In the KPM, a cantilever is used as a reference electrode and the contact potential difference (CPD) between the tip and materials is measured to acquire the work function of the sample and gives information about the Fermi level of a material against vacuum. The Fermi level is sensitive to the degree of doping and a map of it across the material can reveal the spatial distribution of the doping. **Figure 4a** is an atomic force micrograph (AFM) of monolayer WS₂ with a GB. From the AFM scanning image around the GB, the location and the shape of the GB is very easy to tell. Clusters (white dots) with heights of around 10nm accumulate at the GBs. These clusters selectively nucleate on the GBs due to energetics preferences (dangling bonds/strain etc) during the CVD process. Although further experiments are needed to understand the compositions of these clusters, their existence likely impacts the GBs charge transport characteristics. We carried out AFM line scan across the GB in two different positions-one is scanning across a cluster on the GB (red dotted line), the other one is scanning avoiding the clusters (white dotted line). The line profiles of the height are different along these two lines. For the line scan avoiding the clusters, there is no height change when crossing the GB, while for the line with a cluster on it, the height

reaches around 10nm, which means that the intrinsic GB is monolayer, it is the scattered clusters along the GB make it visible.

A typical KPM map for the same WS₂ with a GB is shown in **Figure 4b**. The inset of **Figure 4b** shows the CPD of the tip and WS₂ across the GB (highlighted by the dashed line). The relationship between CPD and the work function of WS₂ can be expressed by the equation: $CPD_{WS_2} = (\phi_{tip} - \phi_{WS_2})/e$, where ϕ_{tip} is the work function of the tip, ϕ_{WS_2} is the work function of WS₂, e is elementary charge. It is evident that the CPD along the GB is higher than the pristine monolayer WS₂ (see **Figure 4b**). This indicates that the work function of pristine WS₂ is higher than at the GBs. In **Figure 4c**, a schematic of the energy band diagram of monolayer WS₂ and GB relative to the AFM tip in their isolated states is shown. The work function at the GB is smaller than that of pristine WS₂, which indicates the Fermi level at GB is higher than the pristine crystal and increased n-doping. **Figure 4d** shows the band profile when the GB and the pristine WS₂ are in contact with each other in an equilibrium state. Band-bending occurs at the interfaces between the GB and the pristine crystal due to varying doping levels. These results substantiate the PL and electrical measurements in underpinning the role of localized doping on charge transport modulation in two dimensional materials with grain boundaries.

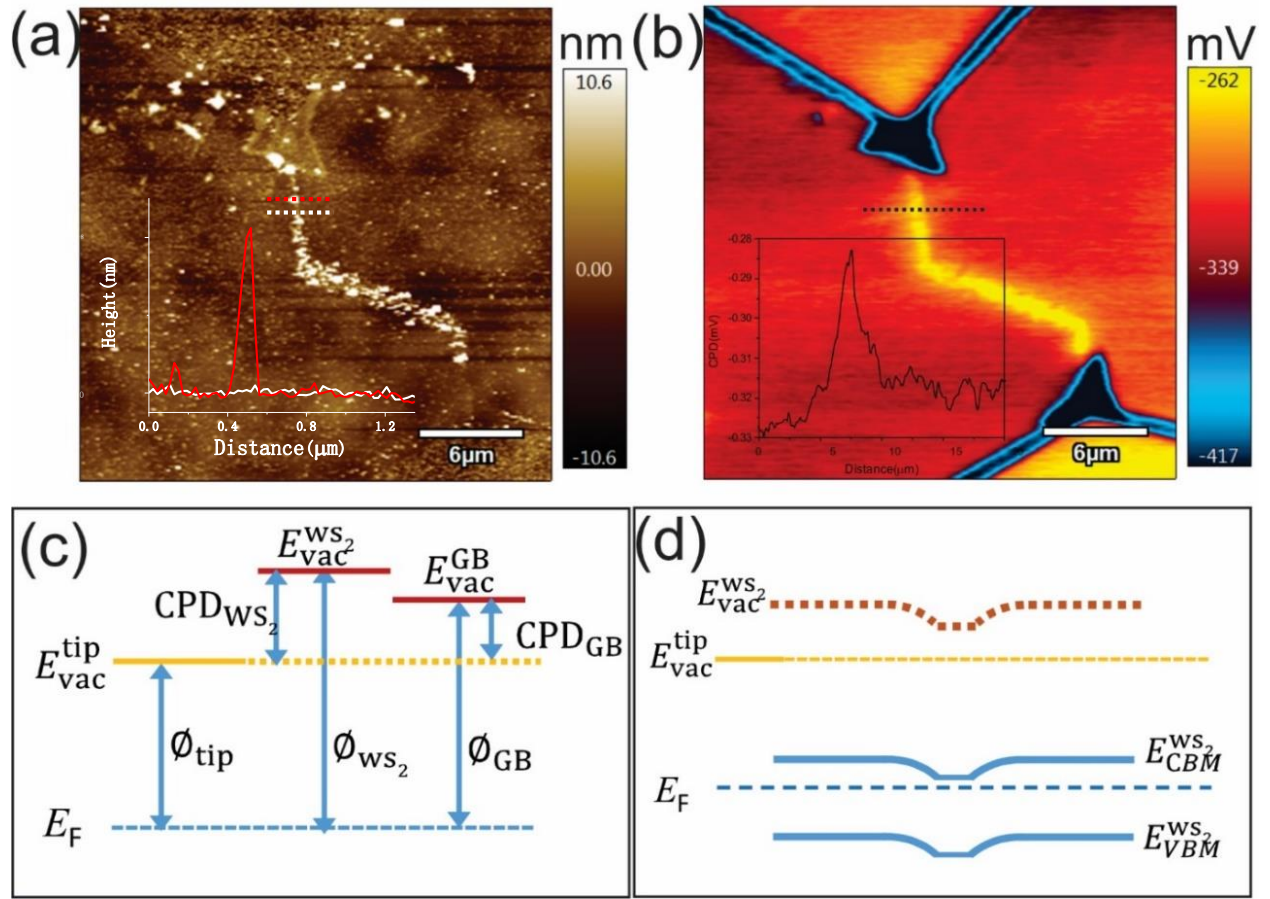


Figure 4. AFM and KPM characterization and energy band diagram. (a) AFM and (b) KPM mapping of WS₂ with a GB. Inset of (a) and (b) are the line profiles of AFM and KPM results along the dashed line across the GB. (c) Schematic of the energy band diagrams of pristine WS₂ and at GB, relative to the KPM tip under equilibrium condition. The yellow solid and dashed lines represent the vacuum level of KPM tip. The red solid lines represent the vacuum level of pristine WS₂ and at GB. The blue dashed line is the fermi level. (d) The energy band diagram with conduction and valance band to show the band bending around the GB.

Conclusion

Efforts to achieve atomic resolution imaging of the WS₂ grain boundaries by transmission electron microscopy were challenging due to the massive domain size and the difficulty in locating GBs within TEM and achieving GBs suspended in free space across holes. Instead we use theoretical calculations to explore the atomic structure of the grain boundaries in the WS₂ monolayer interfaces. To understand the grain boundary formation and structures of WS₂, we extend the previously proposed method of building atomic structures of polycrystalline graphene by combining MD and Monte Carlo (MC) method.⁴⁰ In the method, energetically favored structures are selected by geometries and bond numbers, and further relaxed by MD runs. It can quickly accept or decline the new configuration based on the geometries of defects and has successfully generated well-stitched polycrystalline graphene. In the same way, we iteratively apply a growth algorithm for WS₂ monolayer based on the bond number. Figure 5a presents four steps of the algorithm for the one iteration from a given WS₂ seed to the next seed to be relaxed by MD simulations. Different from graphene, WS₂ has three atoms-thick structures (i). To obtain a correct bond number, we project sulfide atoms positions on flat surfaces by averaging the locations of the top and bottom sulfides, which allows us to calculate the bond number based on the distance between W and S atoms (ii). Then, we add the W or S atoms to the desired position based on newly tuned criterions (iii) will be described in the following section. Finally, we recovered 3D structures from the projected positions for the next structural relaxation MD (iv). We apply NVT ensemble more than 2000 steps with 1fs time step and energy minimization.

The most important part of the growth method is adding or removing the atoms in the step (iii). After we remove the atoms having the bond number more than four, we add atoms only near to the reference atoms having the bond number one or two. If the bond number of the atom is one,

two atoms (W or S, as an opposite type of the reference atoms) are added. If the bond number of the reference atom is two, one atom is added. In this case, if two bonded atoms are the same type, the new atom follows the atom type while if the two bonded atoms are different; the new atom type is randomly selected. We apply the variance on the position of new atoms based on Monte Carlo method. If the distances between the new atom and pre-existing atoms are not long enough, the atoms are rejected. Unlike polycrystalline graphene, there are more kinds of defects at the grain boundary in CVD grown TMD monolayer. We only remove S atoms having bond number two and larger angle than 150° to have reported defect types in previous studies^{23,24,41,42}. The results in figure 5 show the frequently spaced dislocation cores and the meandering nature of the GBs on the nanoscale, figure 5b(ii).

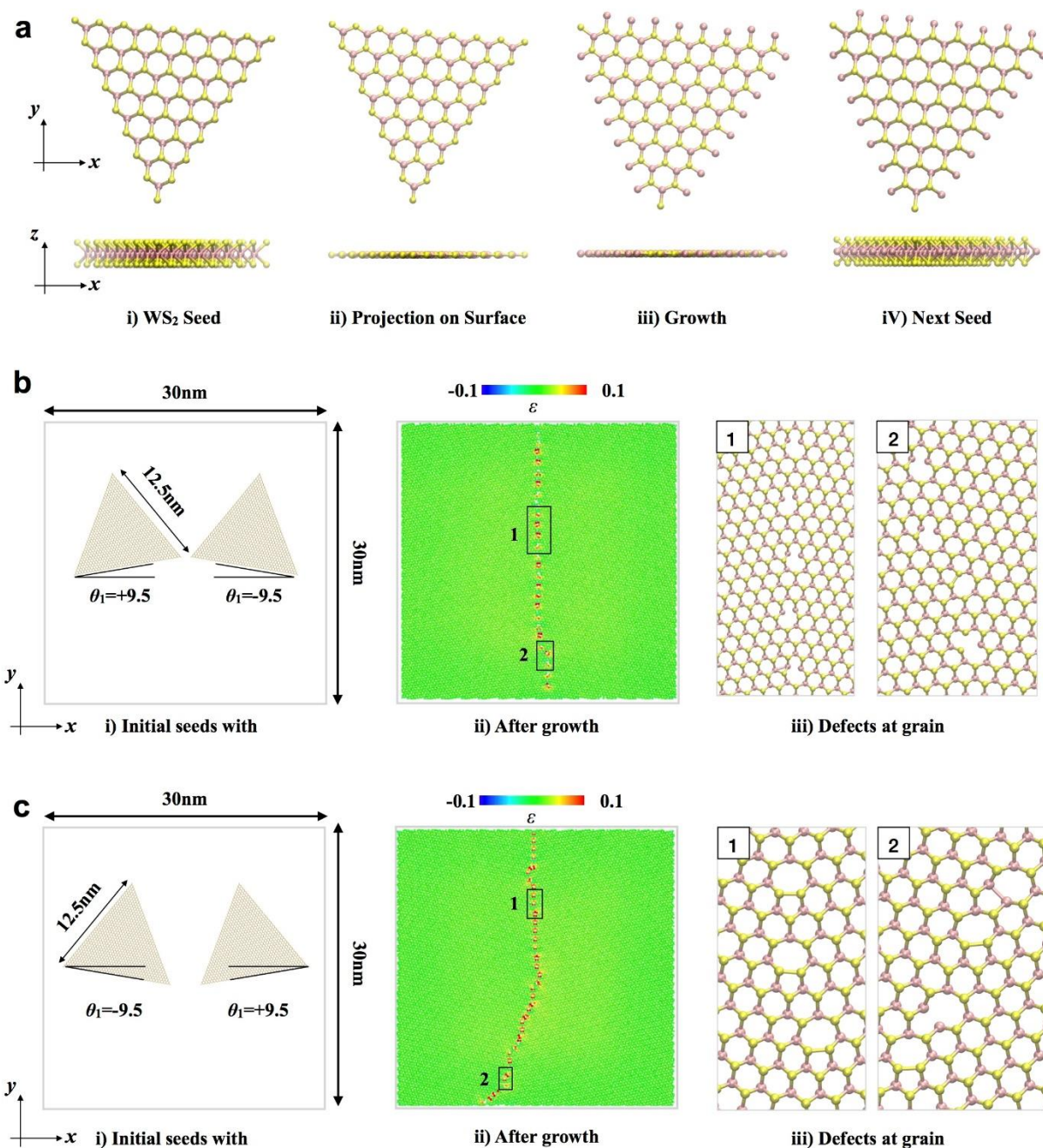


Figure 5. (a) The schematic of the growth algorithm from a relaxed seed of WS_2 (i) to the next seed (iv). To obtain accurate bond information of each atom, the projection the 3D geometries on the flat surface (ii) is required. After adding W or S atoms on the surface (iii), the three-atom-thick structure (iv) is generated from the 2D geometries. (b)-(c) Crystal growth and grain boundary structures with two different angles for 19° mismatching. The supplementary movies show that the angles of initial seed are well controlled during

the growth. The strain (ϵ) is calculated from the relative bond lengths between W-S projected into the x-y plane. The defects at the grain boundary structures are obtained from further relaxation of MD simulations.

Conclusion

In summary, we have studied the effect of grain boundaries on the charge transport characteristics of field-effect transistors based on monolayer WS₂. We find that grain boundaries significantly modulate the electrical behavior of the devices. The modulation is found to be dependent on the orientation of the grain boundaries relative to the channel; with parallel grain boundaries having a negative shift (by 7V), while perpendicular GBs have a positive shift (by 6 V) in the threshold voltage. We find the cause for the modulation to be differential doping levels between the grain boundaries and the pristine crystal, confirmed by photoluminescence spectroscopy and Kelvin probe microscopy experiments. Our results reveal that of grain boundaries can provide conductivity channels within polycrystalline films and dominate when metal electrodes are in direct contact, compared to transport across the GB.

Experimental Methods

CVD Synthesis of Monolayer Graphene and WS₂: WS₂ was synthesized with a two furnace system to control the temperature of S and WO₃ separately. A 2×2 cm silicon chip with 300 nm SiO₂ on top was used as the growth substrate. 300 mg sulfur powder ($\geq 99.5\%$, Sigma-Aldrich) was put in the outer tube, located in the center of first furnace, (inner diameter was 22 mm) while the substrate was 40.5 cm from S powder at the downstream of the same tube. Another precursor, 200 mg WO₃ powder ($\geq 99.5\%$, Sigma-Aldrich) in the inner tube (inner diameter was 12 mm), was in the center of the second furnace and 8.5 cm away from the substrate. Before the reaction started, the system was flushed with 500 sccm Ar for at least 30 min to remove the air inside. The first and second furnaces were then ramped to 180°C and 1170°C at their maximum speed, respectively. The

reaction process lasted for 3 min with Ar flowed at 250 sccm and the two furnaces stable at their set temperatures. The reaction was stopped by decreasing the flow rate of Ar to 10 sccm. Meanwhile, the first furnace was heated at the maximum rising speed to 450 °C to evaporate the rest S and the second one was cooled to room temperature at its maximum cooling speed. When the temperature of second furnace decreased to 950°C, the rest S was blown by Ar at a flow rate of 500 sccm.

Transfer of CVD Synthesized WS₂: The WS₂ was synthesized on SiO₂/Si wafer. A layer of Poly (methyl methacrylate) (PMMA) was spin-coated on WS₂ as the transfer scaffold. The PMMA/WS₂ film was separated from the substrate by etching the SiO₂ with KOH solution (1 mol/L). The PMMA/WS₂ film was then transferred onto deionized water for three times (30 min each time) to remove the remaining KOH. After rinsing, the floating PMMA/WS₂ film were scooped with clean SiO₂/Si substrate and dried overnight at room temperature. Before soaked in acetone to remove PMMA, the samples were heated at 150 °C for 15 min for better adhesion for PMMA/WS₂.

Device Fabrication: For making WS₂ ribbons, one layer of positive photoresist was spin-coated on top of WS₂ before the spin-coating of a layer of negative photoresist to ensure the clean surface of WS₂. JEOL 5500 FS electron beam lithography system was used to write the designed pattern and followed by etching WS₂ with oxygen plasma. For making metal pads, bilayer of positive photoresists were used and Cr (10 nm)/Au (80 nm) were deposited using thermal evaporator, followed by the overnight lift-off in acetone at room temperature.

Electrical and KPM characterization: Two Keithley 2400 source meters were used for electrical measurement and a custom build optical microscope probe station was used to make contact to the metal bond pads. KPM measurements were performed on a MFP-3D atomic force microscope using n-doped Si cantilevers (Olympus/ Resonance frequency- 70 kHz). A two-pass procedure was used to map the surface potentials of the sample: first a topography line in the amplitude-modulated was carried-out in the non-contact mode, followed by the nap-mode for the acquisition of the contact potential difference, done 20 nm above the topography trace.

Molecular Dynamics Simulations for Grain Boundary of WS₂

Molecular dynamics (MD) simulations for crystal growth and grain boundary formation in this study are performed *via* a LAMMPS package.⁴³ We utilize a reactive empirical bond order (REBO) style potential to describe the interatomic interaction of WS₂ monolayer.^{44,45} The parameters of WS₂ have been developed to describe the chemical reactions for the growth of MoS₂ channels embedded in WSe₂ monolayer based on the density functional theory (DFT) calculations with the relative lattice parameters, elastic constants, failure strains, and strengths of transition metal dichalcogenides (TMDs) by adjusting cutoffs and geometric parameters.^{46,47} To obtain the structure of grain boundary with 19° mismatch, we prepare a box of 30nm x 30nm x 10nm space with S edge triangular seeds. The lateral length of triangular seed is 12.5nm. After we apply the growth algorithm with conserving the initial angles of seeds (See Movies 1 and 2, the color legend represents -9.5° to 9.5°), the grain boundaries and defects are obtained in Figure 5b and 5c. We note that a central part of each seed is fixed during the MD relaxation to prevent undesired rotation. Here, the purpose of MD simulations is to catch the structures at the boundary with a specific angle. So, only mirrored seeds are considered in the examples while the relative displacement along the y direction can change the grain boundary to have meandering paths.

Supporting Information

ADF-STEM images of monolayer WS₂ used in these experiments.

Acknowledgements

J.H.W is thankful to the Royal Society and the European Research Council (Grant No: 725258 CoG 2016 LATO) for support. Y. Z. thanks the China Scholarship Council for support. S.G.S

acknowledges a Felix scholarship. The authors thank Youmin Rong for support with the TMD synthesis, and Haijie Tan and Ye Fan for support with device fabrication.

Reference

- (1) Novoselov, K. S.; Geim, A. K.; Morozov, S. V.; Jiang, D. A.; Zhang, Y.; Dubonos, S. V.; Grigorieva, I. V.; Firsov, A. A. Electric Field Effect in Atomically Thin Carbon Films. *Science* **2004**, 306, 666–669.
- (2) Novoselov, K. S.; Geim, A. K.; Morozov, S. V.; Jiang, D.; Katsnelson, M. I.; Grigorieva, I. V.; Dubonos, S. V.; Firsov, A. A. Two-Dimensional Gas of Massless Dirac Fermions in Graphene. *Nature* **2005**, 438, 197–200.
- (3) Hwang, E. H.; Adam, S.; Sarma, S. Das. Carrier Transport in Two-Dimensional Graphene Layers. *Phys. Rev. Lett.* **2007**, 98, 2–5.
- (4) Bonaccorso, F.; Sun, Z.; Hasan, T.; Ferrari, A. C. Graphene Photonics and Optoelectronics. *Nat. Photonics* **2010**, 4, 611–622.
- (5) Nair, R. R.; Blake, P.; Grigorenko, A. N.; Novoselov, K. S.; Booth, T. J.; Stauber, T.; Peres, N. M. R.; Geim, A. K. Fine Structure Constant Defines Visual Transparency of Graphene. *Science* **2008**, 320, 1308.
- (6) Avouris, P. Graphene: Electronic and Photonic Properties and Devices. *Nano Lett.* **2010**, 10, 4285–4294.
- (7) Geim, A. K.; Novoselov, K. S. The Rise of Graphene. *Nat. Mater.* **2007**, 6, 183–191.
- (8) Li, J.; Niu, L.; Zheng, Z.; Yan, F. Photosensitive Graphene Transistors. *Adv. Mater.* **2014**, 26, 5239–5273.
- (9) Meric, I.; Han, M. Y.; Young, A. F.; Oezylmaz, B.; Kim, P.; Shepard, K. L.; Ozyilmaz, B.; Kim, P.; Shepard, K. L. Current Saturation in Zero-Bandgap, Top-Gated Graphene Field-Effect Transistors. *Nat. Nanotechnol.* **2008**, 3, 654–659.
- (10) Lezama, I. G.; Arora, A.; Ubaldini, A.; Barreateau, C.; Giannini, E.; Potemski, M.; Morpurgo, A. F. Indirect-to-Direct Band Gap Crossover in Few-Layer MoTe₂. *Nano Lett.* **2015**, 15, 2336–2342.
- (11) Mak, K. F.; Lee, C.; Hone, J.; Shan, J.; Heinz, T. F. Atomically Thin MoS₂: A New Direct-Gap Semiconductor. *Phys. Rev. Lett.* **2010**, 105, 136805.
- (12) Elías, A. L.; Perea-López, N.; Castro-Beltrán, A.; Berkdemir, A.; Lv, R.; Feng, S.; Long, A. D.; Hayashi, T.; Kim, Y. A.; Endo, M.; Gutierrez, H. R. Controlled Synthesis and Transfer of Large-Area WS₂ Sheets: From Single Layer to Few Layers. *ACS Nano* **2013**, 7, 5235–5242.
- (13) Splendiani, A.; Sun, L.; Zhang, Y.; Li, T.; Kim, J.; Chim, C. Y.; Galli, G.; Wang, F. Emerging Photoluminescence in Monolayer MoS₂. *Nano Lett.* **2010**, 10, 1271–1275.

- (14) Yeh, P. C.; Jin, W.; Zaki, N.; Zhang, D.; Liou, J. T.; Sadowski, J. T.; Al-Mahboob, A.; Dadap, J. I.; Herman, I. P.; Sutter, P.; Osgood Jr, R. M. Layer-Dependent Electronic Structure of an Atomically Heavy Two-Dimensional Dichalcogenide. *Phys. Rev. B-Condens. Matter Mater. Phys.* **2015**, *91*, 1–6.
- (15) Radisavljevic, B.; Radenovic, A.; Brivio, J.; Giacometti, V.; Kis, A. Single-Layer MoS₂ Transistors. *Nat. Nanotechnol.* **2011**, *6*, 147–150.
- (16) Yin, Z.; Li, H.; Li, H.; Jiang, L.; Shi, Y.; Sun, Y.; Lu, G.; Zhang, Q.; Chen, X.; Zhang, H. Single Layer MoS₂ Phototransistors. *ACS Nano* **2012**, *6*, 74–80.
- (17) Zeng, Z.; Yin, Z.; Huang, X.; Li, H.; He, Q.; Lu, G.; Boey, F.; Zhang, H. Single-Layer Semiconducting Nanosheets: High-Yield Preparation and Device Fabrication. *Angew. Chemie-International Ed.* **2011**, *50*, 11093–11097.
- (18) Wang, Q. H.; Kalantar-Zadeh, K.; Kis, A.; Coleman, J. N.; Strano, M. S. Electronics and Optoelectronics of Two-Dimensional Transition Metal Dichalcogenides. *Nat. Nanotechnol.* **2012**, *7*, 699–712.
- (19) Mak, K. F.; He, K.; Shan, J.; Heinz, T. F. Control of Valley Polarization in Monolayer MoS₂ by Optical Helicity. *Nat. Nanotechnol.* **2012**, *7*, 494–498.
- (20) Lee, Y. H.; Zhang, X. Q.; Zhang, W.; Chang, M. T.; Lin, C. T.; Chang, K. D.; Yu, Y. C.; Wang, J. T. W.; Chang, C. S.; Li, L. J.; Lin, T. W. Synthesis of Large-Area MoS₂ Atomic Layers with Chemical Vapor Deposition. *Adv. Mater.* **2012**, *24*, 2320–2325.
- (21) Cong, C.; Shang, J.; Wu, X.; Cao, B.; Peimyoo, N.; Qiu, C.; Sun, L.; Yu, T. Synthesis and Optical Properties of Large-Area Single-Crystalline 2D Semiconductor WS₂ Monolayer from Chemical Vapor Deposition. *Adv. Opt. Mater.* **2014**, *2*, 131–136.
- (22) Zhan, Y.; Liu, Z.; Najmaei, S.; Ajayan, P. M.; Lou, J. Large-Area Vapor-Phase Growth and Characterization of MoS₂ Atomic Layers on a SiO₂ Substrate. *Small* **2012**, *8*, 966–971.
- (23) Van der Zande, A. M.; Huang, P. Y.; Chenet, D. A.; Berkelbach, T. C.; You, Y.; Lee, G. H.; Heinz, T. F.; Reichman, D. R.; Muller, D. A.; Hone, J. C. Grains and Grain Boundaries in Highly Crystalline Monolayer Molybdenum Disulphide. *Nat. Mater.* **2013**, *12*, 554–561.
- (24) Ly, T. H.; Perello, D. J.; Zhao, J.; Deng, Q.; Kim, H.; Han, G. H.; Chae, S. H.; Jeong, H. Y.; Lee, Y. H. Misorientation-Angle-Dependent Electrical Transport across Molybdenum Disulfide Grain Boundaries. *Nat. Commun.* **2016**, *7*, 10426.
- (25) Najmaei, S.; Liu, Z.; Zhou, W.; Zou, X.; Shi, G.; Lei, S.; Yakobson, B. I.; Idrobo, J. C.; Ajayan, P. M.; Lou, J. Vapour Phase Growth and Grain Boundary Structure of Molybdenum Disulphide Atomic Layers. *Nat. Mater.* **2013**, *12*, 754–759.
- (26) Rong, Y.; Fan, Y.; Leen Koh, A.; Robertson, A. W.; He, K.; Wang, S.; Tan, H.; Sinclair, R.; Warner, J. H. Controlling Sulphur Precursor Addition for Large Single Crystal Domains of WS₂. *Nanoscale* **2014**, *6*, 12096–12103.
- (27) Wang, S.; Rong, Y.; Fan, Y.; Pacios, M.; Bhaskaran, H.; He, K.; Warner, J. H. Shape Evolution of Monolayer MoS₂ Crystals Grown by Chemical Vapor Deposition. *Chem. Mater.* **2014**, *26*, 6371–6379.

- (28) Rong, Y.; He, K.; Pacios, M.; Robertson, A. W.; Bhaskaran, H.; Warner, J. H. Controlled Preferential Oxidation of Grain Boundaries in Monolayer Tungsten Disulfide for Direct Optical Imaging-Supporting Information. *ACS Nano* **2015**, *9*, 3695–3703.
- (29) Chang, Y.; Zhang, O. W.; Zhu, O. Y.; Han, Y.; Pu, J.; Chang, J.; Hsu, W. Monolayer MoSe₂ Grown by Chemical Vapor Deposition for Fast Photodetection. *ACS Nano* **2014**, *8*, 8582–8590.
- (30) Scalise, E.; Houssa, M.; Pourtois, G.; Afanas'ev, V.; Stesmans, A. Strain-Induced Semiconductor to Metal Transition in the Two-Dimensional Honeycomb Structure of MoS₂. *Nano Res.* **2012**, *5*, 43–48.
- (31) Bui, V. Q.; Pham, T. T.; Le, D. A.; Thi, C. M.; Le, H. M. A First-Principles Investigation of Various Gas (CO, H₂O, NO, and O₂) Absorptions on a WS₂ Monolayer: Stability and Electronic Properties. *J. Phys. Condens. Matter* **2015**, *27*, 305005.
- (32) Huo, N.; Yang, S.; Wei, Z.; Li, S. S.; Xia, J. B.; Li, J. Photoresponsive and Gas Sensing Field-Effect Transistors Based on Multilayer WS₂ Nanoflakes. *Sci. Rep.* **2014**, *4*, 5209.
- (33) McDonnell, A. S.; Addou, R.; Wallace, R. M.; Hinkle, C. L. Defect Dominated Doping and Contact Resistance in MoS₂. *ACS Nano* **2014**, *8*, 2880–2888.
- (34) Siebel, O. F.; Schneider, M. C.; Galup-Montoro, C. MOSFET Threshold Voltage: Definition, Extraction, and Some Applications. *Microelectronics J.* **2012**, *43*, 329–336.
- (35) Najmaei, S.; Amani, M.; Chin, M. L.; Liu, Z.; Birdwell, A. G.; O'Regan, T. P.; Ajayan, P. M.; Dubey, M.; Lou, J. Electrical Transport Properties of Polycrystalline Monolayer Molybdenum Disulfide. *ACS Nano* **2014**, *8*, 7930–7937.
- (36) Ovchinnikov, D.; Allain, A.; Huang, Y. S.; Dumcenco, D.; Kis, A. Electrical Transport Properties of Single-layer WS₂. *ACS Nano* **2014**, *8*, 8174–8181.
- (37) Dong, L.; Youkey, S.; Bush, J.; Jiao, J.; Dubin, V. M.; Chebiam, R. V. Effects of Local Joule Heating on the Reduction of Contact Resistance Between Carbon Nanotubes and Metal Electrodes. *J. Appl. Phys.* **2007**, *101*, 024320–024327.
- (38) Sarwat, S. G.; Tweedie, M.; Porter, B. F.; Zhou, Y.; Sheng, Y.; Mol, J.; Warner, J. H.; Bhaskaran, H. Revealing Strain-Induced Effects in Ultrathin Heterostructures at the Nanoscale. *Nano Lett.* **2018**, *18*, 2467–2474.
- (39) Zhou, Y.; Tan, H.; Sheng, Y.; Fan, Y.; Xu, W.; Warner, J. H. Utilizing Interlayer Excitons in Bilayer WS₂ for Increased Photovoltaic Response in Ultrathin Graphene Vertical Cross-bar Photodetecting Tunneling Transistors. *ACS Nano*. **2018**, *12*, 4669–4677.
- (40) Jung, G. S.; Qin, Z.; Buehler, M. J., Molecular mechanics of polycrystalline graphene with enhanced fracture toughness. *Extreme Mechanics Letters* **2015**, *2*, 52–59.
- (41) Hong, J.; Hu, Z.; Probert, M.; Li, K.; Lv, D.; Yang, X.; Gu, L.; Mao, N.; Feng, Q.; Xie, L.; Zhang, J.; Wu, D.; Zhang, Z.; Jin, C.; Ji, W.; Zhang, X.; Yuan, J.; Zhang, Z., Exploring Atomic Defects in Molybdenum Disulphide Monolayers. *Nat. Commun.* **2015**, *6*, 6293.
- (42) Azizi, A.; Zou, X.; Ercius, P.; Zhang, Z.; Elías, A. L.; Perea-López, N.; Stone, G.; Terrones,

- M.; Yakobson, B. I.; Alem, N., Dislocation motion and grain boundary migration in two-dimensional tungsten disulphide. *Nat. Commun.* **2014**, 5, 4867.
- (43) Plimpton, S., Fast Parallel Algorithms for Short-Range Molecular Dynamics. *J. Comput. Phys.* **1995**, 117, 1-19.
- (44) Liang, T.; Phillpot, S. R.; Sinnott, S. B., Parametrization of a reactive many-body potential for Mo–S systems. *Phys. Rev. B* **2009**, 79 (24), 245110-14.
- (45) Stewart, J. A.; Spearot, D. E., Atomistic Simulations of Nanoindentation on the Basal Plane of Crystalline Molybdenum Disulfide (MoS_2). *Modell. Simul. Mater. Sci. Eng.* **2013**, 21, 045003-15.
- (46) Han, Y.; Li, M.-Y.; Jung, G.-S.; Marsalis, M. A.; Qin, Z.; Buehler, M. J.; Li, L.-J.; Muller, D. A., Sub-nanometre Channels Embedded in Two-Dimensional Materials. *Nat. Mater.* **2017**, 17, 129-133.
- (47) Jung, G. S.; Wang, S.; Qin, Z.; Martin-Martinez, F. J.; Warner, J. H.; Buehler, M. J., Interlocking Friction Governs the Mechanical Fracture of Bilayer MoS_2 . *ACS Nano* **2018**, 12, 3600-3608.

TOC Graphic

